

## Research Paper

# NIR-II fluorescence microscopic imaging of cortical vasculature in non-human primates

Zhaochong Cai<sup>1\*</sup>, Liang Zhu<sup>2\*</sup>, Mengqi Wang<sup>2</sup>, Anna Wang Roe<sup>3,4,5✉</sup>, Wang Xi<sup>3,4✉</sup>, Jun Qian<sup>1✉</sup>

1. State Key Laboratory of Modern Optical Instrumentations, Centre for Optical and Electromagnetic Research, College of Optical Science and Engineering, Zhejiang University, Hangzhou 310058, China.
2. Interdisciplinary Institute of Neuroscience and Technology (ZIINT), College of Biomedical Engineering and Instrument Science, Zhejiang University, Hangzhou 310027, China.
3. Interdisciplinary Institute of Neuroscience and Technology (ZIINT), the Second Affiliated Hospital, School of Medicine, Zhejiang University, Hangzhou 310020, China.
4. Key Laboratory of Biomedical Engineering of Ministry of Education, College of Biomedical Engineering and Instrument Science, Zhejiang University, Hangzhou 310027, China.
5. Division of Neuroscience, Oregon National Primate Research Center, Oregon Health and Science University, Beaverton, OR 97239, USA.

\*These authors contributed equally

✉ Corresponding authors: qianjun@zju.edu.cn (Jun Qian); xw333@zju.edu.cn (Wang Xi); annawang@zju.edu.cn (Anna Wang Roe)

© The author(s). This is an open access article distributed under the terms of the Creative Commons Attribution License (<https://creativecommons.org/licenses/by/4.0/>). See <http://ivyspring.com/terms> for full terms and conditions.

Received: 2019.12.31; Accepted: 2020.02.18; Published: 2020.03.04

## Abstract

Vasculature architecture of the brain can provide revealing information about mental and neurological function and disease. Fluorescence imaging in the second near-infrared (NIR-II) regime with less light scattering is a more promising method for detecting cortical vessels than traditional visible and NIR-I modes.

**Methods:** Clinically approved dye indocyanine green (ICG) was used for NIR-II fluorescence imaging. Here, for the first time, we developed two NIR-II fluorescence microscopy systems for brain vasculature imaging in macaque monkeys. The first is a wide-field microscope with high temporal resolution for measuring blood flow velocity and cardiac impulse period, while the second is a high spatial resolution confocal microscope producing three-dimensional maps of the cortical microvascular network. Both were designed with flexibility to image various cortical locations on the head.

**Results:** Here, ICG was proved to have high brightness in NIR-II region and an 8-fold QY increase in serum than in water. We achieved cerebrovascular functional imaging of monkey with high temporal resolution (25 frames/second) with wide-field microscope. The blood flow velocity of capillaries can be precisely calculated and the cardiac impulse period can be monitored as well. *In vivo* structural imaging of cerebrovasculature was accomplished with both high spatial lateral resolution (~8  $\mu\text{m}$ ) and high signal to background ratio (SBR). Vivid 3D reconstructed NIR-II fluorescence confocal microscopic images up to depth of 470  $\mu\text{m}$  were also realized.

**Conclusion:** This work comprises an important advance towards studies of neurovascular coupling, stroke, and other diseases relevant to neurovascular health in humans.

Key words: NIR-II fluorescence imaging, non-human primates, indocyanine green, cortical vasculature, confocal imaging

## Introduction

Fluorescence bioimaging is a sensitive, non-invasive and radiation-free technology that is capable of revealing biological structure and function [1]. Its utility has been demonstrated in clinical applications, such as imaging-guided surgery for liver

tumors and retinal angiography [2,3]. However, its application for studying microvascular architecture and function in the human brain has not been well developed. There is now rapidly growing recognition that health of brain vasculature is essential for normal

neurological and mental function. In particular, the role of fine microvasculature is proving to be a critical component in meeting the oxygen and energy demands of normal neuronal function [4-7]. The decline of vascular health can disrupt neurovascular coupling, leading to oxygen delivery mismatches and resulting functional decline. Indeed, common neurological disorders such as Alzheimer's or ALS (amyotrophic lateral sclerosis) may be rooted in disorders of vascular structure and/or function [8,9]. The purpose of this study is to develop a fluorescence microscopic imaging methodology for studying vascular architecture and function for future clinical application.

A traditional way to image vasculature is based on fluorescence signals whose wavelength is in the visible spectral range (400–760 nm) or first near-infrared (NIR-I) spectral region (760–900 nm) [10]. Both methods have small tissue penetration depth and low spatial resolution due to the severe scattering of fluorescence photons by biological tissues [11]. A more recent development, fluorescence bioimaging in the second near-infrared spectral region (NIR-II), takes advantage of emission wavelengths in the 900–1700 nm spectral range. This fluorescence bioimaging method utilizes long-wavelength and low-scattering signals, providing larger penetration depth and higher spatial resolution than visible or NIR-I fluorescence bioimaging [12]. Given that biological tissue usually has low autofluorescence in the long wavelength regime, NIR-II fluorescence bioimaging also provides high SBR [13].

These advantages have made NIR-II fluorescence bioimaging a method of choice for functional applications in mice, including whole-body angiography, organ visualization, as well as diagnosis and imaging-guided treatment of tumours [10-12, 14-31]. With respect to brain vasculature, NIR-II fluorescence microscopy has been used in studies of vascular structural architecture and blood flow velocity of mice [32]. Such studies in mice have been extremely exciting and have pushed forward the field. However, given the significant differences in structural and functional aspects of brain vasculature in mice vs humans, developing NIR-II fluorescence microscopy for human clinical use still requires development.

Here, to enable future clinical applications, we have developed NIR-II methods for brain microangiography in the rhesus macaque monkey, an animal model with cortical structure and organization similar to humans. One significant difference between primates (both human and nonhuman primates) and mice is that much of the cerebral cortex is organized into modular functional units of integrated neuronal

response (termed columns or domains) [33-35]. This primate-specific functional architecture suggests that there may be specializations of vascular architecture to meet the metabolic and hemodynamic demands of columnar unit-based response, a possibility that is receiving growing attention [36-39]. As a step towards clinical application, our goal was thus to develop a method appropriate for the nonhuman primate, one that meets the needs of studying vascular structure and function. We aimed to achieve high lateral spatial resolution for observing even the smallest vessels (5-10  $\mu\text{m}$ ), high temporal resolution for monitoring blood flow (up to 0.65 mm/s) in capillaries, and depth of imaging permitting visualization of the superficial layers of the cerebral cortex. Moreover, we intend this method to be relatively easy to use and at moderate cost, important for developing a practical and robust tool for clinical use.

Here, we report the development of two NIR-II fluorescence microscopes adapted to brain imaging of large animals. Using a clinically approved dye named indocyanine green (ICG) as a bright NIR-II fluorescent probe [40,41] in rhesus macaques, we demonstrate that the wide-field NIR-II fluorescence microscope offers high temporal resolution [32], sufficient for realizing real-time imaging of cerebral blood vessels and achieving measurement of cerebral blood flow (CBF) velocity and cardiac cycle. The second microscope, a confocal NIR-II fluorescence microscope, offers high lateral spatial resolution and high SBR via optical sectioning capability [42], enabling reconstruction of a clear three-dimensional volume of cortical vasculature up to an imaging depth of  $\sim 500 \mu\text{m}$ . Capillary vessels with a diameter less than 7  $\mu\text{m}$  could be resolved.

## Results

### Optical characterization of ICG in rhesus macaque serum

Key to clinical feasibility is the availability and applicability of safe and effective labelling agents. Thus far, several types of NIR-II fluorescent probes, including carbon nanotubes [43], rare-earth doped nanoparticles [44], quantum dots [45], small-molecule organic dyes [46] and organic nanoparticles [47,48], have been utilized for *in vivo* imaging of small animals. However, these probes have not been developed for human use. To work towards a capability that is easily compatible with human use, we utilized ICG (Figure 1A), a probe that is readily available and is approved by US Food and Drug Administration (FDA). ICG has been previously used in humans as a typical NIR-I fluorophore (for studies of liver and retina) [2,3,49], and, as been previously

shown, also offers the advantage of bright NIR-II fluorescence emission [40].

Prior to *in vivo* applications in imaging cortical vasculature of rhesus macaques, we first evaluated the optical characteristics of ICG in rhesus macaque serum (RMS). We found two important benefits of ICG. First, by comparing the absorption spectra of ICG in water with that in RMS (Figure 1B), we observed that the absorption of ICG in RMS peaked at 806 nm, a wavelength that is red-shifted ~30 nm compared to that of ICG in water. This enhanced absorbance in RMS (in the range of 786–888 nm) significantly increases the excitation efficiency of 793 nm laser, important for the feasibility of following *in vivo* confocal microscopic imaging in primates. Second, we found that the normalized fluorescence spectra (Figure 1C) of ICG in RMS showed an emission peak at ~900 nm, which is ~60 nm red-shifted compared to ICG in water. This increases greatly the portion of fluorescence emission in NIR-II

spectral region (shaded region of graph). Moreover, a NIR-II fluorescence quantum yield (QY) of ICG in RMS reaches 4.1%, which is a dramatic increase of 8.2-fold compared to ICG in water (Figure 1D); this is also higher than most other NIR-II fluorescent probes [43,44,46,50]. The increased absorbance and QY result in striking improvements in signal brightness as seen through the NIR-II fluorescence wide-field microscope (Figure 1E, left panels, 98% increase) and confocal microscopic imaging results (Figure 1E, right panels, 214% increase). These unique optical features of ICG in RMS are due to the fact that ICG molecules (molecular size less than 0.5 nm) tend to adsorb on serum proteins and form an “organic dye-protein complex” (Supplementary Figure 1), which thus contributes to the red-shift of absorption and emission spectra, as well as reduces the aggregation-caused quenching (ACQ) effect of ICG arising from its self-aggregation in water [22,51–53].

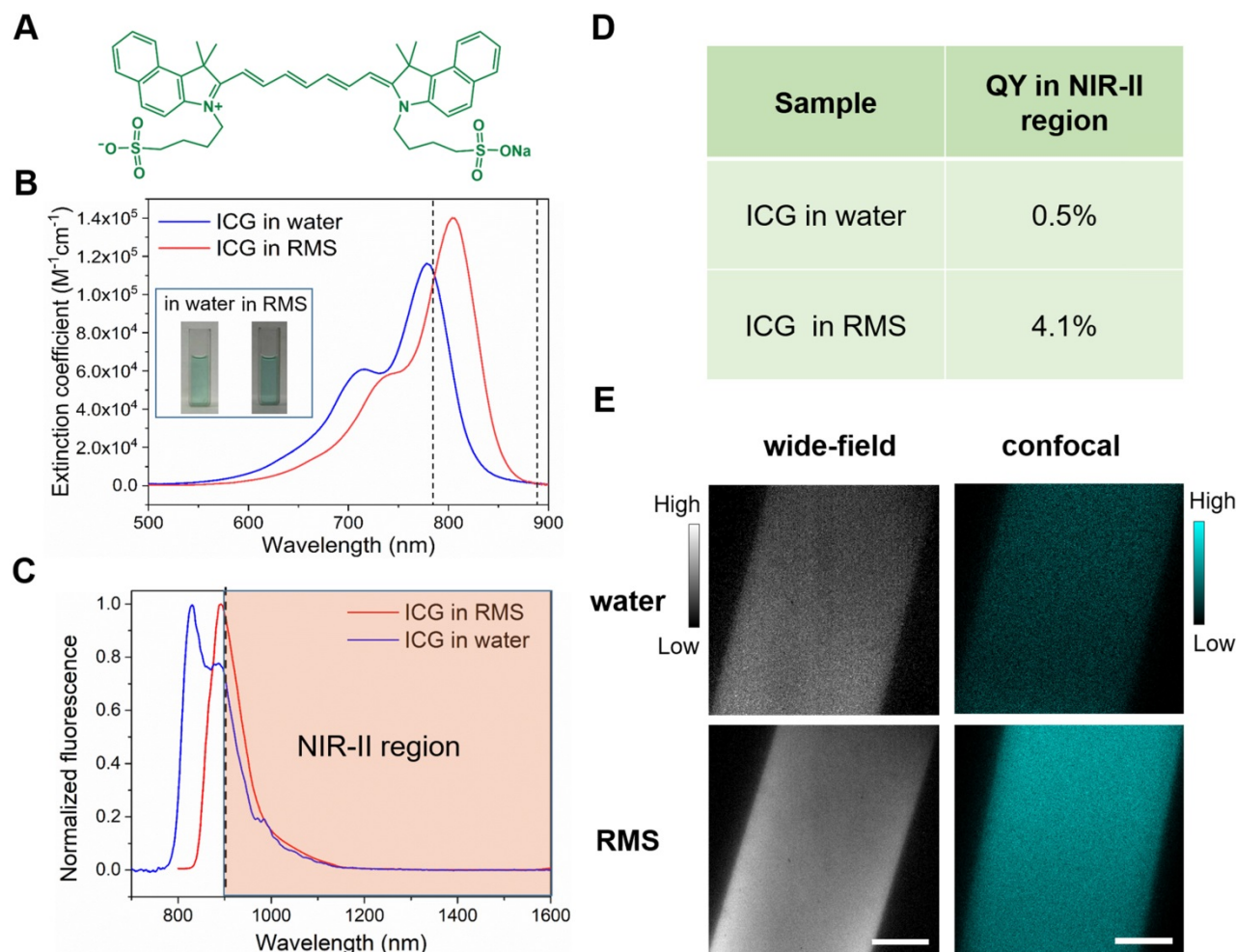


**Figure 1.** Optical characterization of ICG in RMS. **A** Molecular structure of ICG. **B** The extinction coefficient spectra of ICG in water (blue) and RMS (red). Concentration: 0.01 mg/mL. Inset: bright-field images of ICG in water and RMS. Dashed lines: range of increased absorbance in RMS. **C** Normalized fluorescence spectra of ICG in water and RMS. Shaded region: fluorescence spectrum of ICG in RMS beyond 900 nm. **D** NIR-II fluorescence QY of ICG in water and ICG in RMS. An 808 nm laser was used as the excitation source. The fluorescence signals (900–1650 nm, the fluorescence proportion of ICG in 1650–1700 nm is negligible) were collected by an integrating sphere and detected by an InGaAs sensor. **E** Images of ICG in water and RMS from NIR-II fluorescence wide-field microscope (left panels, 780 nm LED excitation) and confocal microscope (right panels, 793 nm laser excitation). Scale bars: 100  $\mu$ m.

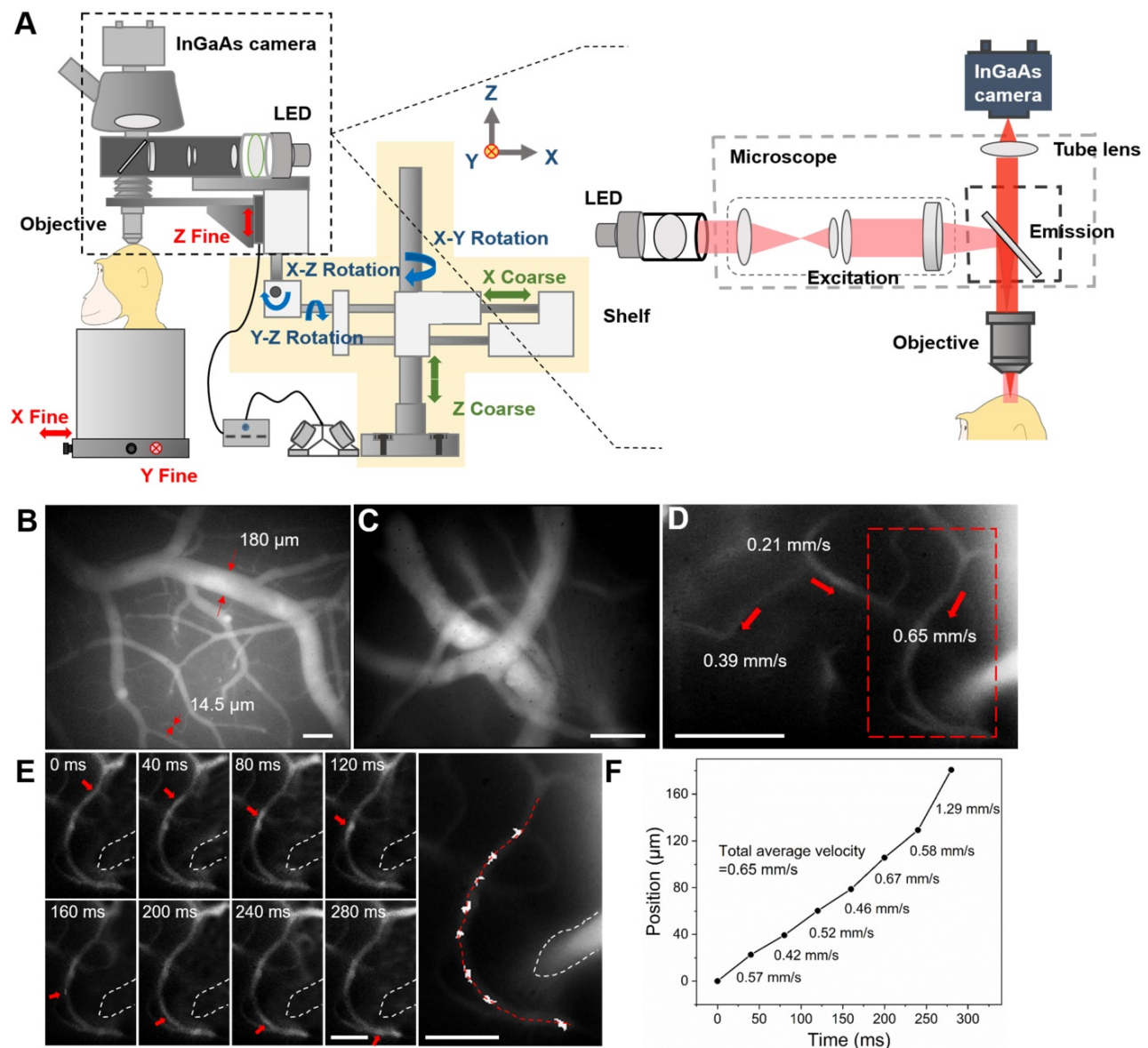


**Figure 2.** *In vivo* fluorescence wide-field microscopic imaging of cerebral blood vessels of the rhesus macaque in the NIR-II spectral region. **A** Schematic illustration of the custom NIR-II fluorescence wide-field microscopic imaging system. Red arrows: fine adjustment. Blue arrows: rotation. Green arrows: coarse adjustment. The excitation and imaging light paths are shown on the right panel. **B** A typical microscopic image of brain blood vessels with low magnification ( $\sim 3\times$ ). **C** A typical microscopic image of brain blood vessels with high magnification ( $\sim 25\times$ ). **D** Blood flow velocities in three sampled vessels. Velocity calculation shown in **E**, **F**. Red arrows indicate the directions of blood flow. Dashed red box: region shown in **E**. **E** Frames showing tracking a fluorescent point in a capillary (diameter =  $8\ \mu\text{m}$ ). The figure on the right marks the tracked positions. **F** A plot of the position of the point as a function of time. The average velocities between two consecutive frames are shown on the right of the line. The total average velocity ( $0.65\ \text{mm/s}$ ) is calculated based on the seven average velocities. Excitation wavelength:  $780\ \text{nm}$ . Excitation power (before the objective):  $\sim 69\ \text{mW}$ . Exposure time of the InGaAs camera:  $10\ \text{ms}$ . Scale bars in **B**, **C** and **D**:  $100\ \mu\text{m}$ , scale bars in **E**:  $50\ \mu\text{m}$ .

### ***In vivo* NIR-II fluorescence wide-field microscopic imaging of cerebral blood vessels of rhesus macaques**

NIR-II fluorescence wide-field microscopy offers high temporal resolution and easy operation, which are features of traditional wide-field fluorescence microscopy. In addition, due to the minimal scattering of fluorescence signals in biological tissues, NIR-II fluorescence wide-field microscopy achieves larger penetration depth. Though there have been several reports on *in vivo* NIR-II fluorescence wide-field microscopic imaging in mice (e.g. brain and tumour

angiography) [32,50,54], such imaging on large animals has never been demonstrated. To establish such a capability, we custom-designed a NIR-II fluorescence wide-field microscopic system.

The configuration of our lab-built optical setup is shown in Figure 2A. A  $780\ \text{nm}$  LED was coupled to a microscope illuminator and utilized as the excitation source. NIR-II fluorescence images were collected by an NIR anti-reflection objective and recorded with an InGaAs camera. One challenge for imaging large animal brains is that, unlike mice, their cranial windows are not always horizontal. Due to the large brain size, areas of interest may lie in planes of

antero-posterior or mediolateral tilt. To address this need, we mounted the whole optical system on a multi-direction adjustable shelf (yellow shaded area in Figure 2A), thereby enabling convenient translation and rotation, as demonstrated by the straight (green) and curved (blue) arrows. This permitted positioning of the objective directly above and perpendicular to the cranial window. In addition, for micropositioning of the field of view (FOV) during imaging (red arrows), the rhesus macaque was placed on a stage which could be moved in the x-y plane. For fine z-direction adjustment, the objective was fixed on a motor-driven electric module capable of a 10  $\mu\text{m}$  step-by-step tomographic imaging. This instrument was also designed with the potential of imaging in awake, behaving primates with head-fixation.

Following implantation of a cranial window under anesthesia (see Methods), ICG was intravenously injected (1.43 mg/kg, below clinical safe dose of 5 mg/kg [55]) and the brain was imaged through the custom NIR-II fluorescence microscope. A low-magnification objective ( $\sim 3\times$ ) was first used to provide a structural map of cerebral blood vessels (Figure 2B). Due to the large FOV (2.1 $\times$ 1.7 mm) and bright NIR-II fluorescence signals from ICG, both large blood vessels (diameter=180  $\mu\text{m}$ ) and microcapillaries (diameter=14.5  $\mu\text{m}$ ) could be visualized simultaneously. This map was then used to select and focus on a specific sub-ROI via a  $\sim 25\times$  objective for obtaining a higher-resolution image of blood vessels (Figure 2C, depth= 130  $\mu\text{m}$ ).

Our next goal was to understand functional aspects of the vascular network by studying the flow within different sized vessels. Under the  $\sim 25\times$  objective, numerous bright points from NIR-II fluorescence emission of ICG were observed moving along capillaries (Figure 2D and Supplementary MOV S1). Under baseline conditions (e.g. under anesthesia), flow velocity within single microvessels should be stable. To calculate CBF velocity, a single point on a capillary was selected (Figure 2D, red dashed box) and continuously tracked at 25 frames per second (FPS) (Figure 2E). As shown in Figure 2F, by plotting the positions of this point at different frames, we determined a CBF average velocity of 0.65 mm/s for this fine vessel. The blood flow velocities in other two capillaries within the FOV were also determined in the same way (0.21 mm/s and 0.39 mm/s, red arrows in Figure 2d). In this way, the flow characteristics of multiple capillaries in a FOV could be evaluated at the same time. Since veins collect blood from branches while arteries distribute blood into branches [37], blood vessel type (vein or artery) could be recognized according to the flow direction (Supplementary Figure 2 and Supplementary MOV S2).

In the z direction, blood vessels at various depths were imaged (Supplementary Figure 3). The images at two typical depths were analyzed and the results illustrated the microcapillaries could be resolved (FWHM = 7.8 $\mu\text{m}$  at the depth of 300 $\mu\text{m}$  and FWHM=8.5 $\mu\text{m}$  at the depth of 170 $\mu\text{m}$ , Supplementary Figure 4). Nevertheless, since “wide-field excitation and area detection” imaging mode was adopted, the fluorescence signals both above and below the focal plane of objective were also recorded and became the background of the image on the focal plane, which reduced the SBR of imaging.

In addition, in some large blood vessels, regions with bright/dark borders were clearly observed oscillating in position over time with cardiac impulse (Supplementary MOV S3 clearly shows this border pulsation). Supplementary Figure 5a illustrates the highest (top panel) and the lowest (bottom panel) position of the bright/dark border during one cardiac impulse period. The fluctuation of the bright/dark border position is displayed in Supplementary Figure 5B. By plotting the timepoints of peaks of each pulse and making a linear fit, a pulse rate of 2 Hz was obtained (Supplementary Figure 5C). This calculated period was consistent with that concurrently measured by the physiological monitor (120 pulses per minute). This demonstrates that the high temporal resolution of NIR-II fluorescence wide-field microscopy provides simultaneous pulse rate information from large vessels while monitoring blood flow velocity in small vessels; these are parameters which are likely to prove useful in studies of vascular flow and hemodynamics.

### **In vivo NIR-II fluorescence confocal microscopic imaging of cerebral blood vessels of rhesus macaques**

Although our NIR-II fluorescence wide-field microscopy was capable of realizing real-time brain imaging on rhesus macaques, its spatial resolution and SBR were inevitably influenced by out-of-focus signals (fluorescence signals both above and below the focal plane of objective). To address this challenge, we turned to NIR-II fluorescence confocal microscopy, which offers fine optical sectioning and high SBR, as well as large penetration depth from NIR-II fluorescence bioimaging, as demonstrated by *ex vivo* and *in vivo* bioimaging in mice [17,45,56-58]. To achieve this capability in large animals, we custom-designed a NIR-II fluorescence confocal microscopic system, modified from our previous lab-built setup [42,50]. As shown in Figure 3A, to achieve point detection of NIR-II fluorescence signals, we used a 793 nm laser as the excitation source and an InGaAs photomultiplier tube (PMT) with high QY at

900-1700 nm wavelengths. A multimode fiber with a core diameter of 400  $\mu\text{m}$  played the role of a pinhole to exclude the out-of-focus signals (signals produced outside the focus of excitation laser). The galvanometers inside the scan unit could achieve fine point-by-point scanning in the x-y direction. The vertical position of the objective was adjusted by a motor-driven electric module to realize fine

step-by-step (10  $\mu\text{m}$ ) z-direction movement. The whole confocal microscopic system was fixed on a multi-direction adjustable shelf, which permitted accurate positioning via convenient translation and rotation of the objective directly above and perpendicular to the cranial window (red arrows in Figure 3A). The subject was placed on a stage which could be moved in the x-y direction prior to imaging.

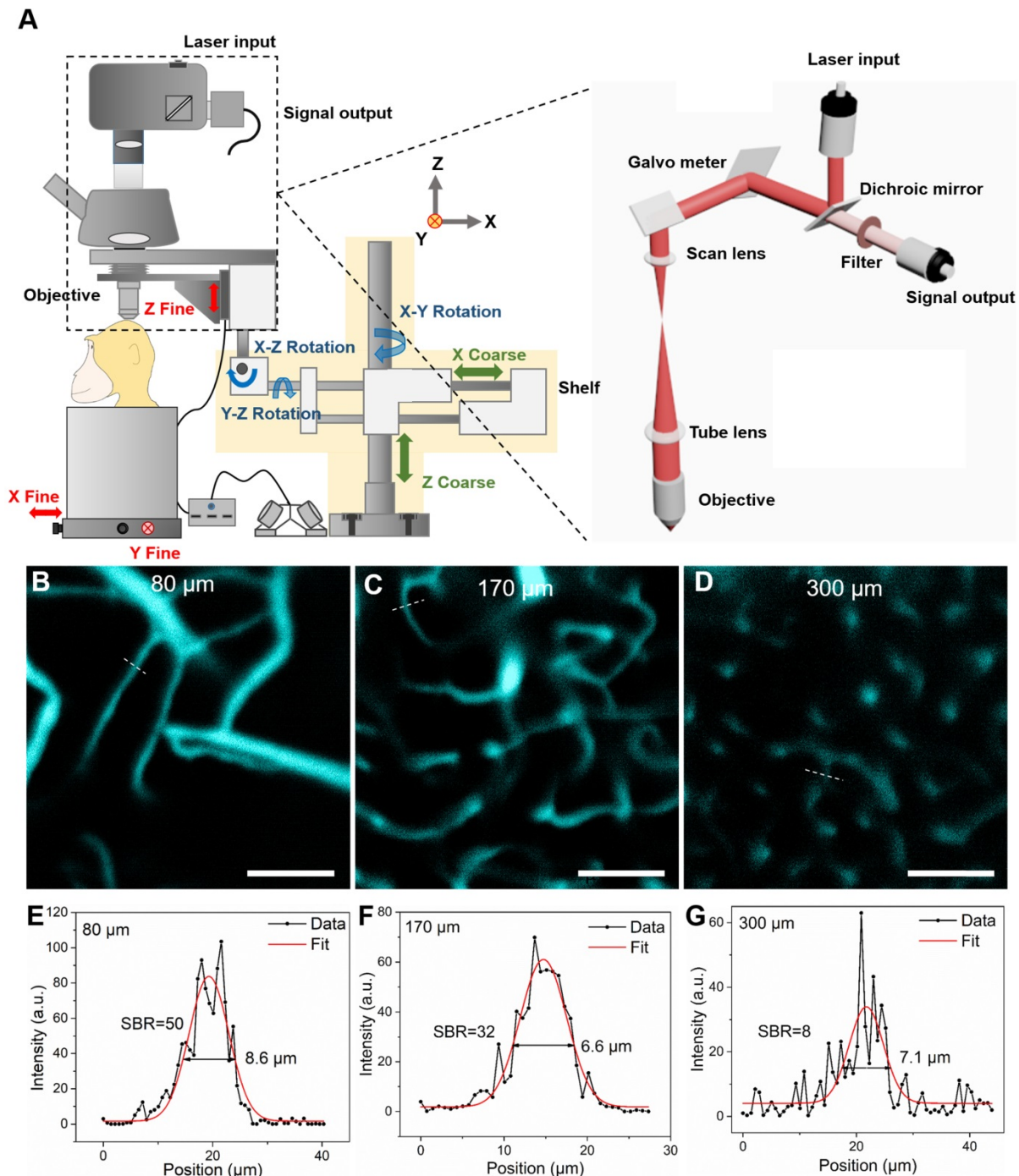


**Figure 3.** NIR-II fluorescence confocal microscopic *in vivo* imaging of cerebral blood vessels of the rhesus macaque with high lateral resolution and SBR. **A** The schematic illustration of the NIR-II fluorescence confocal microscopic imaging system. Red arrows: fine adjustment. Blue arrows: rotation. Green arrows: coarse adjustment. The excitation and imaging light paths are showed on the right panel. **B-D** NIR-II fluorescence confocal microscopic images at three typical depths (80  $\mu\text{m}$ , 170  $\mu\text{m}$  and 300  $\mu\text{m}$ ). White dashed lines: locations of cross-sections depicted in **E-G**. **E-G** The cross-sectional fluorescence intensity profiles (black) and the related Gaussian fits (red) along the capillary vessels, taken from locations (white-dashed lines) in **B-D**. Excitation wavelength: 793 nm. Laser power:  $\sim 40$  mW before the objective. PMT voltage:  $\sim 531$  V. Pinhole diameter: 400  $\mu\text{m}$ . All scale bars: 100  $\mu\text{m}$ .

Prior to monkey experiments, in order to test the performance of the optical system, confocal brain imaging was first performed on mice. Results in supplementary Figures 6 and 7 demonstrate the setup worked well. Next, *in vivo* cerebral cortical vessel imaging on the rhesus macaques was implemented (injected dose of ICG was 2.86 mg/kg, below clinical safe dose of 5 mg/kg). Due to the bright NIR-II fluorescence emission of ICG in RMS and the spatial filtering capability of NIR-II fluorescence confocal microscope, we achieved high lateral resolution and high SBR of the cortical vascular network (Figure 3). Figure 3B~D are representative confocal images taken at depth of 80  $\mu\text{m}$ , 170  $\mu\text{m}$  and 300  $\mu\text{m}$ , respectively, showing clear vascular morphology. In Figure 3E~G, profiles and Gaussian fits of fluorescence intensity profiles along the white dashed lines in Figure 3B~D are shown. At a depth of 170  $\mu\text{m}$  (Fig 3c), the SBR was as high as 32, permitting vessels as small as 6.6  $\mu\text{m}$  in diameter (FWHM) to be resolved. Even at a depth of 300  $\mu\text{m}$ , the SBR of 8 was achieved, providing clear images of a capillary vessel with a diameter (FWHM) of 7.1  $\mu\text{m}$ . Thus, in comparison to NIR-II fluorescence wide-field microscopy (Supplementary Figure 4), the greatly improved SBRs (2.1 at the depth of 170  $\mu\text{m}$  and

1.5 at the depth of 300  $\mu\text{m}$ ) produced spatially resolved images of capillaries at good penetration depths.

Tomographic imaging of cerebral blood vessels was further conducted with a step resolution of 10  $\mu\text{m}$ . The reconstructed images at various depths (0-130 $\mu\text{m}$ , 140-250  $\mu\text{m}$  and 260-470  $\mu\text{m}$ ) are shown in Figure 4A~C, where the cerebral blood vessels of rhesus macaque showed clear and distinct layers. By reconstructing the images, a vivid 3D vascular architecture was obtained (Figure 4D, Figure 4E and Supplementary MOV S4). A maximal imaging depth of 470  $\mu\text{m}$  could still be obtained, thanks to the “NIR-I excitation and NIR-II emission” imaging mode. In comparison to the NIR-II fluorescence wide-field microscopy, NIR-II fluorescence confocal microscopy possessed higher SBR and lateral spatial resolution, though at the price of lower temporal resolution (5.24 s per picture). Despite this, a scanning speed of 20  $\mu\text{s}$ /pixel was achieved, a speed still much faster than that (50  $\mu\text{s}$ /pixel) achieved in other studies in mice [17]. We conclude that our NIR-II fluorescence confocal microscope is capable of high lateral spatial resolution 3D imaging of vascular networks in rhesus macaques.

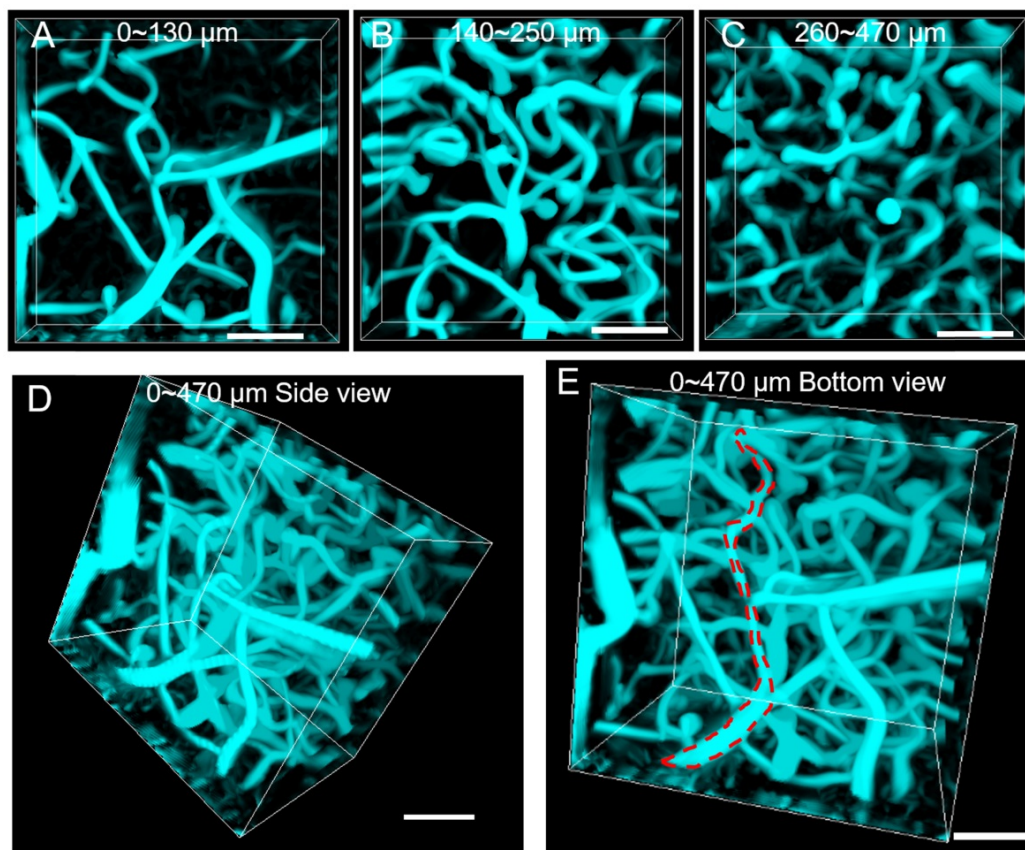


**Figure 4.** NIR-II fluorescence confocal microscopic *in vivo* imaging of cerebral blood vessels of the rhesus macaque with large penetration depth. (A-C) 3D reconstructed NIR-II fluorescence confocal microscopic images of brain blood vessels at various depths (A: 0-130  $\mu\text{m}$ , B: 140-250  $\mu\text{m}$ , C: 260-470  $\mu\text{m}$ ). (D-E) 3D reconstructed NIR-II fluorescence confocal microscopic images up to depth of 470  $\mu\text{m}$  from the side view D and bottom view E. Red dashed lines in E: outline of single vessel. All the images were generated through Maximum Intensity Projection mode. Excitation wavelength: 793 nm. Laser power: ~40 mW before the objective. PMT voltage: ~531 V. Pinhole diameter: 400  $\mu\text{m}$ . All scale bars: 100  $\mu\text{m}$ .

## Discussion

### A new method for high spatial and temporal resolution angiography in primates

In this study, we provide a promising NIR-II fluorescent approach for cortical angiography in nonhuman primates. For the first time, we conducted *in vivo* NIR-II fluorescence bioimaging of cerebral cortical microvasculature in rhesus macaques. To achieve structural and functional imaging on cerebral vascular network, we specifically designed two NIR-II fluorescence microscopes. Both of them adopted NIR-I light source to reduce the tissue-absorption of excitation, and used the InGaAs detector to collect NIR-II signals with a minimum of tissue-scattering, thereby enabling large imaging depth. The NIR-II fluorescence wide-field microscope adopted the “area-excitation and area-detection” approach, which offered advantages of high temporal resolution and easy operation. The NIR-II fluorescence confocal microscope was based on “point-excitation, point-detection and spatial filtering”, with advantages of fine optical sectioning and high SBR.

In addition, we designed the microscopes so that they could image the brain at different angles, to permit study through cranial windows in different cortical areas of interest in rhesus macaques. Such flexibility will also prove valuable for future studies in awake, behaving monkeys. To overcome these difficulties, both microscopes were fixed on a multi-direction adjustable shelf, where translation and rotation were enabled and the objective angle and position could be flexibly adjusted above and perpendicular to the cranial window. In addition, the rhesus macaque was placed on a large and stable stage, where precise x-y movement was enabled. As far as we know, these are the first NIR-II fluorescence microscopes for *in vivo* imaging in non-human primates.

### Probe that is clinically compatible and bright

In addition to the development of the NIR-II fluorescence microscopic systems, NIR-II fluorescent probes were also critical for successful imaging in non-human primates. These probes must satisfy at least three requirements. The first is their bio-safety. Similar to humans, the experimental ethics must be carefully considered. ICG, which was approved by FDA in 1958 [59], has been safely utilized in various clinical applications, and should also have negligible toxicity in rhesus macaques. Thus, the use of biocompatible fluorescent probes are an essential feature and test of this method. A second requirement is that the probe must have sufficiently high brightness in NIR-II spectral region. This is important

for obtaining higher temporal and spatial resolution, as well as reducing the excitation intensity and other parameters (e.g. imaging time) of the imaging instruments. Finally, to permit application of the needed volumes in large animals (such as rhesus macaques which weigh 5-7 kg), the fluorescent probes should be easily accessible and not too costly [60]. The medical ICG we adopted was commercially available (in hospitals), more readily available than all the other reported NIR-II fluorescent probes, and moderate in cost. Thus, unlike carbon nanotubes, rare-earth doped nanoparticles, quantum dots, small-molecule organic dyes, and organic nanoparticles, these requirements are readily met by ICG.

We further learned that ICG is optically advantageous for use in nonhuman primates. As a typical kind of NIR-I fluorescent probe [49], ICG has been proven to exhibit bright NIR-II fluorescence [40,61], and it has extremely large absorbance and has been successfully employed for NIR-II fluorescence functional bioimaging in mice. We determined that the absorbance of ICG in RMS increased in the spectral region between 786 nm and 888 nm, compared to that of ICG in water. In addition, we measured a dramatic 8.2-fold increase of the NIR-II fluorescence QY of ICG in RMS compared to that of ICG in water. Thus, under the excitation of 780 nm LED (for wide-field microscope) or 793 nm laser (for confocal microscope), ICG in RMS exhibited much brighter NIR-II emission, making it ideal for *in vivo* cerebral blood vessel imaging of nonhuman primates.

### Implications and significance

We believe that there are important implications of a primate-compatible method for imaging fine vascular networks. The role of fine vasculature is central to both normal brain function and brain disease. For example, the fine capillary bed and associated precapillary arterioles are believed to be the center of essential oxygen delivery to cortical neurons [37]. Normal hemodynamic function may be dependent on distribution of vascular control points and key temporal control of local constriction and dilation in response to metabolic demand [4,5]. Unlike mice, in primates and humans, many cortical areas are organized in so-called cortical columns, which are units of coherent neuronal function [33-35]. However, what the organizing principle of this coherence is still under investigation. The coherence of neuronal response suggests that the column may be a unit of oxygen demand, one which is potentially related to the modular architecture of vascular networks. In addition, as feedforward vs feedback cortical processes central to cognitive control are organized in differential laminar fashion [62], understanding the

laminar organization of microvasculature may be key to the cortical processes [63]. Thus, it is critical to have a method for studying architectural and functional aspects of the microvascular network in both the columnar and laminar dimensions in nonhuman primates. This capability will advance our understanding of human neurovascular function in normal brain function and in neurological and mental disease.

## Methods

### Materials

ICG was purchased from Dandong Yichuang Pharmaceutical Co. Ltd. China. Phosphate-buffered saline (PBS) was obtained from Sinopharm Chemical Reagent Co. Ltd. China.

### Optical characterization of ICG

Absorption spectra of ICG were obtained with a UV-vis-NIR scanning spectrophotometer (UV2550, Shimadzu, Japan). Fluorescence spectra were measured by a NIR spectrometer (FLS980, Edinburgh instruments, UK). Absolute NIR-II fluorescence quantum yield was directly measured by a QY measuring instrument (Quantaaurus-QY C13534, Hamamatsu, Japan).

### Animals

All experimental procedures conducted in mice and monkeys were approved by the Institutional Animal Care and Use Committee of Zhejiang University and in accordance with the National Institutes of Health Guidelines. Male C57BL6/J mice (Jackson Labs; 9-10 weeks old) were housed at 24°C with a normal 12 h light/dark cycle, and fed with water and food *ad libitum*. In our study, three healthy adult male rhesus macaques (4-5 years old and weighing 5-7 kg) were used, and they were housed at the Nonhuman Primate Facility at Zhejiang University.

### Monkey surgical procedure

Rhesus macaques were anesthetized with ketamine hydrochloride (10 mg/kg)/atropine (0.03 mg/kg) and maintained with propofol (5 mg/kg per hour iv; induction, 5 mg/kg) or sufentanil (2 to 4 µg/kg per hour iv; induction, 3 µg/kg) supplemented with isoflurane (0.5 to 2%). Animals were intubated and artificially ventilated. End-tidal CO<sub>2</sub>, respiration rate, SpO<sub>2</sub>, heart rate, electrocardiogram and rectal temperature were continuously monitored and maintained. The end-tidal CO<sub>2</sub> was kept around 4% by adjusting the rate and volume of the ventilator, and the rectal temperature of 37.5°C to 38.5°C was maintained by an animal warming system. To access the cerebral cortex, we designed and made the quartz

glass window according to literature [64]. A quartz glass coverslip (diameter=12 mm, thickness=0.17 mm) was glued in a metal ring (diameter=8 mm, thickness=2 mm) with silicone adhesive. The skull and dura were opened to expose the cortex. Then this window unit was gently pushed down onto the cortical surface. The edge of the glass was inserted under the dura and the metal ring was glued with skull with dental cement to form an imaging chamber. This provided sufficient cortical stabilization for imaging. Following head fixation and prior to NIR-II fluorescence imaging, ICG was injected intravenously through the saphenous vein (~2 mg/kg) to label the vasculature. Following completion of surgical and experimental procedures, monkeys were recovered and provided analgesics.

### NIR-II fluorescence wide-field microscopic imaging

A lab-built optical system was established to conduct NIR-II fluorescence wide-field microscopic brain imaging on the rhesus macaques. A 780 nm LED (M780L3-C1, Thorlabs, USA) was used as the excitation source. Reflected by a 900 nm long-pass (LP) dichroic mirror (DMLP900R, Thorlabs) and passing through an air objective lens (LSM03, working distance (WD) = 25.1 mm, Thorlabs) or an infrared anti-reflection water-immersed objective lens (XLPLN25XWMP2, 25×, numerical aperture (NA) = 1.05, Olympus, Japan), the 780 nm beam illuminated onto the brain of the rhesus macaque. The excited NIR-II fluorescence was collected by the same objective lens, passing through the same 900 nm LP dichroic mirror and a 900 nm LP filter (FELH0900, Thorlabs), and finally was recorded by an InGaAs camera (SW640, Tekwin, China) via a built-in tube lens in a triocular (BX51, Olympus). The objective was fixed on a motor-driven electric module (ZFM2020, Thorlabs) and could be moved in the Z axis to focus at different depths of the brain. The whole microscope was fixed on a multi-direction adjustable shelf, which permitted careful positioning of the objective right above the window. A flexible translation and rotation system permitted precise position of the microscope perpendicular to the cranial window. In addition, placement of the rhesus macaque on an independently controlled stage provided precise x-y movement when conducting imaging.

### NIR-II fluorescence confocal microscopic imaging

A lab-built optical system was set to perform NIR-II fluorescence confocal microscopic brain imaging on the rhesus macaques. A 793 nm continuous-wave (CW) laser (Rugkuta Optoelectron-

ics, China) beam was introduced into a scan unit (Thorlabs) and then reflected by a 900 nm LP dichroic mirror (DMLP900R, Thorlabs). After passing through the galvanometers, scan lens and tube lens, the excitation light was focused on the cranial window of rhesus macaque by an infrared anti-reflection water-immersed objective lens (XLPLN25XWMP2, 25×, NA = 1.05, Olympus). The emitting NIR-II fluorescence passed the aforementioned light path (from the 900 nm LP dichroic mirror to the objective) in counter direction, as well as a 900 nm LP filter (FELH0900, Thorlabs), and was finally directed into a NIR sensitive InGaAs PMT (H12397-75, Hamamatsu) through a multimode fiber. The pinhole size depended on the aperture (core diameter) of this fiber, which, in this case was 400 μm. The output electric signal from the PMT was amplified with an amplifier (C12319, Hamamatsu) and acquired images reconstructed. Similar to the NIR-II fluorescence wide-field microscope, the objective was fixed on the motor-driven electric module (ZFM2020, Thorlabs) and the laser excitation beam could be focused at different depths of the cortex. The whole microscope was also fixed on the multi-direction adjustable shelf, enabling precise adjustment of the position between objective and the cranial window of the rhesus macaque. Animals (rhesus macaques or mice) were placed on an independently controlled stage, and fine point-by-point scanning in x-y direction was achieved via galvanometers.

### Image analysis

All data analyses were performed using MATLAB (R2018b; MathWorks) and IMARIS (Oxford Instruments). For vessels 3D reconstruction, images were processed with Simple Non Local Means (NLM) Filter (Christian Desrosiers, <https://ww2.mathworks.cn/matlabcentral/fileexchange/52018-simple-non-local-means-nlm-filter>) to reduce noise, and were enhanced structures in 2D images using hessian eigenvalues by Jerman Enhancement Filter (Tim Jerman, <https://ww2.mathworks.cn/matlabcentral/fileexchange/63171-jerman-enhancement-filter>). For processed images, IMARIS 3D Surfaces were used to precisely rebuild the 3D network map (Maximum Intensity Projection) of blood vessels. In order to track the movements of bright points in the capillaries, the original images were subtracted to the average image of all the frames and the Matlab image tool box was used to obtain the bright points positions in each frames.

### Abbreviations

ACQ: aggregation-caused quenching; ALS: amyotrophic lateral sclerosis; CBF: cerebral blood

flow; CW: continuous-wave; FDA: US Food and Drug Administration; FOV: field of view; ICG: indocyanine green; LP: long-pass; NA: numerical aperture; NIR: near infrared; NIR-I: the first near-infrared; NIR-II: the second near-infrared; NLM: non local means; PBS: phosphate-buffered saline; PMT: photomultiplier tube; QY: quantum yield; RMS: rhesus macaques serum; ROI: region of interest; SBR: signal to background ratio; WD: working distance.

### Supplementary Material

Supplementary figures and movie legends.

<http://www.thno.org/v10p4265s1.pdf>

Supplementary movie 1.

<http://www.thno.org/v10p4265s2.avi>

Supplementary movie 2.

<http://www.thno.org/v10p4265s3.avi>

Supplementary movie 3.

<http://www.thno.org/v10p4265s4.avi>

Supplementary movie 4.

<http://www.thno.org/v10p4265s5.avi>

### Acknowledgements

This work was supported by National Natural Science Foundation of China (61735016, 81430010, 61975172, 81702508, 91632105, 31627802), Zhejiang Provincial Natural Science Foundation of China (LR17F050001, LY17C090005) and the Fundamental Research Funds for the Central Universities (2019QNA5001).

### Competing Interests

The authors have declared that no competing interest exists.

### References

- Prasad PN. Introduction to biophotonics. New Jersey, USA: John Wiley & Sons; 2003.
- Ishizawa T, Fukushima N, Shibahara J, Masuda K, Tamura S, Aoki T, et al. Real-time identification of liver cancers by using indocyanine green fluorescent imaging. *Cancer*. 2009; 115: 2491-504.
- Novotny HR, Alvis DL. A method of photographing fluorescence in circulating blood in the human retina. *Circulation*. 1961; 24: 82-6.
- Attwell D, Buchan AM, Charpak S, Lauritzen M, MacVicar BA, Newman EA. Glial and neuronal control of brain blood flow. *Nature*. 2010; 468: 232-43.
- Andreone BJ, Lacoste B, Gu C. Neuronal and vascular interactions. *Annu Rev Neurosci*. 2015; 38: 25-46.
- Iadecola C. The neurovascular unit coming of age: a journey through neurovascular coupling in health and disease. *Neuron*. 2017; 96: 17-42.
- Blinder P, Tsai PS, Kaufhold JP, Knutsen PM, Suhl H, Kleinfeld D. The cortical angiome: an interconnected vascular network with noncolumnar patterns of blood flow. *Nat Neurosci*. 2013; 16: 889-97.
- Kisler K, Nelson AR, Montagne A, Zlokovic BV. Cerebral blood flow regulation and neurovascular dysfunction in Alzheimer disease. *Nat Rev Neurosci*. 2017; 18: 419-34.
- Zlokovic BV. Neurovascular pathways to neurodegeneration in Alzheimer's disease and other disorders. *Nat Rev Neurosci*. 2011; 12: 723-38.
- Hong G, Antaris AL, Dai H. Near-infrared fluorophores for biomedical imaging. *Nat Biomed Eng*. 2017; 1: 10.

11. Hong G, Diao S, Chang J, Antaris AL, Chen C, Zhang B, et al. Through-skull fluorescence imaging of the brain in a new near-infrared window. *Nat Photonics*. 2014; 8: 723-30.
12. Hong G, Lee JC, Robinson JT, Raaz U, Xie L, Huang NF, et al. Multifunctional in vivo vascular imaging using near-infrared II fluorescence. *Nat Med*. 2012; 18: 1841-6.
13. Diao S, Hong G, Antaris AL, Blackburn JL, Cheng K, Cheng Z, et al. Biological imaging without autofluorescence in the second near-infrared region. *Nano Res*. 2015; 8: 3027-34.
14. Wang P, Fan Y, Lu L, Liu L, Fan L, Zhao M, et al. NIR-II nanoprobes in-vivo assembly to improve image-guided surgery for metastatic ovarian cancer. *Nat Commun*. 2018; 9: 2810-98.
15. Hong G, Robinson JT, Zhang Y, Diao S, Antaris AL, Wang Q, et al. In vivo fluorescence imaging with Ag<sub>2</sub>S quantum dots in the second near-infrared region. *Angew Chem Int Ed*. 2012; 51: 9818-21.
16. Chen Y, Montana DM, Wei H, Cordero JM, Schneider M, Le Guevel X, et al. Shortwave infrared in vivo imaging with gold nanoclusters. *Nano Lett*. 2017; 17: 6330-4.
17. Wan H, Yue J, Zhu S, Uno T, Zhang X, Yang Q, et al. A bright organic NIR-II nanofluorophore for three-dimensional imaging into biological tissues. *Nat Commun*. 2018; 9: 1171.
18. Hong G, Zou Y, Antaris AL, Diao S, Wu D, Cheng K, et al. Ultrafast fluorescence imaging in vivo with conjugated polymer fluorophores in the second near-infrared window. *Nat Commun*. 2014; 5: 4206.
19. Li D, Wang D, Zhao X, Xi W, Zebibula A, Alifu N, et al. Short-wave infrared emitted/excited fluorescence from carbon dots and preliminary applications in bioimaging. *Mater Chem Front*. 2018; 2: 1343-50.
20. Zebibula A, Alifu N, Xia L, Sun C, Yu X, Xue D, et al. Ultrastable and biocompatible NIR-II quantum dots for functional bioimaging. *Adv Funct Mater*. 2018; 28: 1703451.
21. Zeng X, Xiao Y, Lin J, Li S, Zhou H, Nong J, et al. Near-Infrared II dye-protein complex for biomedical imaging and imaging-guided photothermal therapy. *Adv Healthc Mater*. 2018; 7: 1800589.
22. Antaris AL, Chen H, Diao S, Ma Z, Zhang Z, Zhu S, et al. A high quantum yield molecule-protein complex fluorophore for near-infrared II imaging. *Nat Commun*. 2017; 8: 15269.
23. Guo B, Chen J, Chen N, Middha E, Xu S, Pan Y, et al. High-resolution 3D NIR-II photoacoustic imaging of cerebral and tumor vasculatures using conjugated polymer nanoparticles as contrast agent. *Adv Mater*. 2019; 31: 1808355.
24. Zhu S, Yung BC, Chandra S, Niu G, Antaris AL, Chen X. Near-infrared-II (NIR-II) bioimaging via off-peak NIR-I fluorescence emission. *Theranostics*. 2018; 8: 4141-51.
25. Meng X, Zhang J, Sun Z, Zhou L, Deng G, Li S, et al. Hypoxia-triggered single molecule probe for high-contrast NIR II/PA tumor imaging and robust photothermal therapy. *Theranostics*. 2018; 8: 6025-34.
26. Hu X, Tang Y, Hu Y, Lu F, Lu X, Wang Y, et al. Gadolinium-chelated conjugated polymer-based nanotheranostics for photoacoustic/magnetic resonance/NIR-II fluorescence imaging-guided cancer photothermal therapy. *Theranostics*. 2019; 9: 4168-81.
27. Li X, Jiang M, Zeng S, Liu H. Polydopamine coated multifunctional lanthanide theranostic agent for vascular malformation and tumor vessel imaging beyond 1500 nm and imaging-guided photothermal therapy. *Theranostics*. 2019; 9: 3866-78.
28. Wang P, Wang X, Luo Q, Li Y, Lin X, Fan L, et al. Fabrication of red blood cell-based multimodal theranostic probes for second near-infrared window fluorescence imaging-guided tumor surgery and photodynamic therapy. *Theranostics*. 2019; 9: 369-80.
29. Wang Y, Zhang W, Sun P, Cai Y, Xu W, Fan Q, et al. A novel multimodal NIR-II nanoprobe for the detection of metastatic lymph nodes and targeting chemo-photothermal therapy in oral squamous cell carcinoma. *Theranostics*. 2019; 9: 391-404.
30. Deng G, Li S, Sun Z, Li W, Zhou L, Zhang J, et al. Near-infrared fluorescence imaging in the largely unexplored window of 900-1,000 nm. *Theranostics*. 2018; 8: 4116-28.
31. Wu K, Zhao H, Sun Z, Wang B, Tang X, Dai Y, et al. Endogenous oxygen generating multifunctional theranostic nanoplateform for enhanced photodynamic-photothermal therapy and multimodal imaging. *Theranostics*. 2019; 9: 7697-713.
32. Qi J, Sun C, Zebibula A, Zhang H, Kwok RTK, Zhao X, et al. Real-time and high-resolution bioimaging with bright aggregation-induced emission dots in short-wave infrared region. *Adv Mater*. 2018; 30: 1706856.
33. Hubel DH, Wiesel TN. Ferrier lecture. Functional architecture of macaque monkey visual cortex. *Proc R Soc Lond B*. 1977; 198: 1-59.
34. Rakic P. Specification of cerebral cortical areas. *Science*. 1988; 241: 170-6.
35. Mountcastle VB. The columnar organization of the neocortex. *Brain*. 1997; 120: 701-22.
36. Wang Z, Roe AW. Columnar specificity of microvascular oxygenation and blood flow response in primary visual cortex: evaluation by local field potential and spiking activity. *J Cereb Blood Flow Metab*. 2012; 32: 6-16.
37. Sakadzic S, Mandeville ET, Gagnon L, Musacchia JJ, Yaseen MA, Yucel MA, et al. Large arteriolar component of oxygen delivery implies a safe margin of oxygen supply to cerebral tissue. *Nat Commun*. 2014; 5: 5734.
38. Keller AL, Schuez A, Logothetis NK, Weber B. Vascularization of cytochrome oxidase-rich blobs in the primary visual cortex of squirrel and macaque monkeys. *J Neurosci*. 2011; 31: 1246-53.
39. Schmid F, Barrett MJP, Jenny P, Weber B. Vascular density and distribution in neocortex. *Neuroimage*. 2019; 197: 792-805.
40. Carr JA, Franke D, Caram JR, Perkinson CF, Saif M, Askoxylakis V, et al. Shortwave infrared fluorescence imaging with the clinically approved near-infrared dye indocyanine green. *Proc Natl Acad Sci U S A*. 2018; 115: 4465-70.
41. Landsman ML, Kwant G, Mook GA, Zijlstra WG. Light-absorbing properties, stability, and spectral stabilization of indocyanine green. *J Appl Physiol*. 1976; 40: 575-83.
42. Yu W, Guo B, Zhang H, Zhou J, Yu X, Zhu L, et al. NIR-II fluorescence in vivo confocal microscopy with aggregation-induced emission dots. *Sci Bull*. 2019; 64: 410-6.
43. Diao S, Blackburn JL, Hong G, Antaris AL, Chang J, Wu JZ, et al. Fluorescence imaging in vivo at wavelengths beyond 1500 nm. *Angew Chem Int Ed*. 2015; 54: 14758-62.
44. Zhong Y, Ma Z, Zhu S, Yue J, Zhang M, Antaris AL, et al. Boosting the down-shifting luminescence of rare-earth nanocrystals for biological imaging beyond 1500 nm. *Nat Commun*. 2017; 8: 737.
45. Zhang M, Yue J, Cui R, Ma Z, Wan H, Wang F, et al. Bright quantum dots emitting at approximately 1,600 nm in the NIR-IIb window for deep tissue fluorescence imaging. *Proc Natl Acad Sci U S A*. 2018; 115: 6590-5.
46. Antaris AL, Chen H, Cheng K, Sun Y, Hong G, Qu C, et al. A small-molecule dye for NIR-II imaging. *Nat Mater*. 2016; 15: 235-42.
47. Alifu N, Zebibula A, Qi J, Zhang H, Sun C, Yu X, et al. Single-molecular near-infrared-II theranostic systems: ultrastable aggregation-induced emission nanoparticles for long-term tracing and efficient photothermal therapy. *ACS Nano*. 2018; 12: 11282-93.
48. Guo B, Feng Z, Hu D, Xu S, Middha E, Pan Y, et al. Precise deciphering of brain vasculatures and microscopic tumors with dual NIR-II fluorescence and photoacoustic imaging. *Adv Mater*. 2019; 31: 1902504.
49. Marshall MV, Rasmussen JC, Tan IC, Aldrich MB, Adams KE, Wang X, et al. Near-infrared fluorescence imaging in humans with indocyanine green: a review and update. *Open Surg Oncol J*. 2010; 2: 12.
50. Feng Z, Yu X, Jiang M, Zhu L, Zhang Y, Yang W, et al. Excretable IR-820 for in vivo NIR-II fluorescence cerebrovascular imaging and photothermal therapy of subcutaneous tumor. *Theranostics*. 2019; 9: 5706-19.
51. Desmettre T, Devoisselle JM, Mordon S. Fluorescence properties and metabolic features of indocyanine green (ICG) as related to angiography. *Surv Ophthalmol*. 2000; 45: 15-27.
52. Magata M, Kubota T. Molecular interaction and electronic spectra. New York, USA: Dekker; 1970.
53. Deshpande AV, Beidoun A, Penzkofer A, Wagenblast G. Spectroscopic investigation of cyanovinyl-diethylaniline dyes in solutions. *Chem Phys*. 1990; 148: 141-54.
54. Bruns OT, Bischof TS, Harris DK, Franke D, Shi Y, Riedemann L, et al. Next-generation in vivo optical imaging with short-wave infrared quantum dots. *Nat Biomed Eng*. 2017; 1: 56.
55. Alander JT, Kaartinen I, Laakso A, Pätälä T, Spillmann T, Tuchin VV, et al. A review of indocyanine green fluorescent imaging in surgery. *Int J Biomed Imaging*. 2012; 2012: 1-26.
56. Zhu S, Yang Q, Antaris AL, Yue J, Ma Z, Wang H, et al. Molecular imaging of biological systems with a clickable dye in the broad 800- to 1,700-nm near-infrared window. *Proc Natl Acad Sci U S A*. 2017; 114: 962-7.
57. Zhu S, Herrai S, Yue J, Zhang M, Wan H, Yang Q, et al. 3D NIR-II molecular imaging distinguishes targeted organs with high-performance NIR-II bioconjugates. *Adv Mater*. 2018; 30: e1705799.
58. Liu C, Liao J, Chen L, Chen J, Ding R, Gong X, et al. The integrated high-resolution reflection-mode photoacoustic and fluorescence confocal microscopy. *Photoacoustics*. 2019; 14: 12-8.
59. Fox IJ, Wood EH. Indocyanine green: physical and physiologic properties. *Mayo Clin Proc*. 1960; 35: 732.
60. Ma Z, Wan H, Wang W, Zhang X, Uno T, Yang Q, et al. A theranostic agent for cancer therapy and imaging in the second near-infrared window. *Nano Res*. 2019; 12: 273-9.
61. Starosolski Z, Bhavane R, Ghaghada KB, Vasudevan SA, Kaay A, Annapragada A. Indocyanine green fluorescence in second near-infrared (NIR-II) window. *PLoS One*. 2017; 12: e187563.

62. Felleman DJ, Van Essen DC. Distributed hierarchical processing in the primate cerebral cortex. *Cereb Cortex*. 1991; 1: 1-47.
63. Adams DL, Valentina P, Economides JR, Horton JC. Vascular supply of the cerebral cortex is specialized for cell layers but not columns. *Cereb Cortex*. 2015; 25: 3673-81.
64. Li M, Liu F, Jiang H, Lee TS, Tang S. Long-term two-photon imaging in awake macaque monkey. *Neuron*. 2017; 93: 1049-57.